Progress In Electromagnetics Research, Vol. 182, 107–119, 2025

(Received 17 December 2024, Accepted 26 February 2025, Scheduled 7 March 2025)

Geometrical Modeling and Experimental Measurements of Indoor mmWave Communication Systems Including Finite-Area Reflective Surfaces

Viacheslav Ivanov[1,*], Alexander Volkov[1], and David R. Peters[2]

[1] *Corning SAS Finland, Salmisaarenaukio 1, 00180 Helsinki, Finland*
[2] *Corning Research and Development Corporation, SP-ZV-01, 21 Lynn Morse Drive, 14870 Painted Post, NY, USA*

ABSTRACT: This work, for the first time to our knowledge, describes in detail the incorporation of the numerical and semi-analytical intelligent reflector scattering models into the modelling framework of the state-of-art dual-polarization three-dimensional geometrical channel models, where propagation channel impact and antennas impact are separated. The proposed formalism allows indoor coverage impact studies of the meta reflectors in mmWave and THz radio communication systems. The model considers reflector phase-design, near-field effects, polarization transformations, incident beam patterns, multipath and diffraction effects, and is confirmed by full-wave simulations and measurements.

1. INTRODUCTION

The high path losses at high radio frequencies drive application of the beamforming techniques in the mmWave and THz remote nodes (RNs). The presence of walls introduces signal blockages and/or attenuation, resulting in non-line of sight (NLOS) propagation between a serving RN and mobile phone user equipment (UE). In NLOS areas, the received power is decreased compared to the line-of-sight (LOS) areas, further limiting coverage. Beamforming has its own limitations too, such as the maximum sizes of antenna arrays and poor radiation efficiency for extreme steering angles, all of which drive the exploration of intelligent reflectors.

One of the implementations of the intelligent meta-reflectors for radio frequency applications is a passive meta-reflector, which is a plate composed of a ground plane and dielectric layer, on top of which conductor elements are placed in a subwavelength lattice as shown in Fig. 1. The unit cells of the lattice may have very different specially designed structures, which vary across the surface to modify shape of the scattered wavefront. The total size of the surface might be on the order of several tens or hundreds of wavelengths. A definitive tutorial on meta-reflectors is given in [1] and [2].

There have been numerous papers addressing passive reflectors inclusion in wireless channel modeling. Reviewed modeling formalisms can be classified into two types — those applying semi-analytical approaches (phased-array or aperture models) and those reusing electromagnetic simulation results. In [3], for an L-shaped corridor, the analytical expressions of the received signal power after reflection from passive surface were given and validated against ray tracing using software [4] and measurements. The analytics included first- and second order reflections, despite not considering meta-reflectors particularly and their scattering patterns. In [5], the authors proposed a model, which allows including polarization-dependent meta-reflector scattering patterns for double-hop LOS links, with accurate tracking of azimuth and zenith angles of departure and arrival. However, multipath propagation was not considered, and reflector scattering patterns were extracted from electromagnetic simulations only. In [6], the phase-shift distribution concept for meta-reflector scattering pattern prediction was presented and analytical expressions of the reflected power contribution were derived, but only for two-dimensional incidence and reflection and single polarization. In [7], a phased array approach was applied to 10 GHz reflector designs and considered generalized expressions for scattering fields given both azimuth and zenith angles variation of scattering pattern and dual polarization for a LOS propagation path. Multipath propagation however was not considered in that work. In [8], a review of various phased array modeling approaches of meta-reflectors was conducted. The authors proposed an extension to account for diffraction grating effect of the meta-reflectors via Bloch-Floquet theorem and introduced the average dielectric constant and modulation index parameters of the surface. The expressions for amplitudes of the Floquet modes are provided in the MATLAB code in [9]. In [10], the authors extended the model for non-planar incident waves, given the antennas description. In [11], the authors presented an effective algorithm for coverage modelling with meta-reflectors, where reflector is considered as a secondary source. Neither of these two papers however considered channel impact and antennas impact separation and thus had to be further adapted for thorough compatibility with 3GPP-like channel models [12], which would allow reusing the same computed channel for different antenna types

---

[*] Corresponding author: Viacheslav Ivanov (IvanovVV@Corning.com).

doi:10.2528/PIER24121703

Published by THE ELECTROMAGNETIC ACADEMY

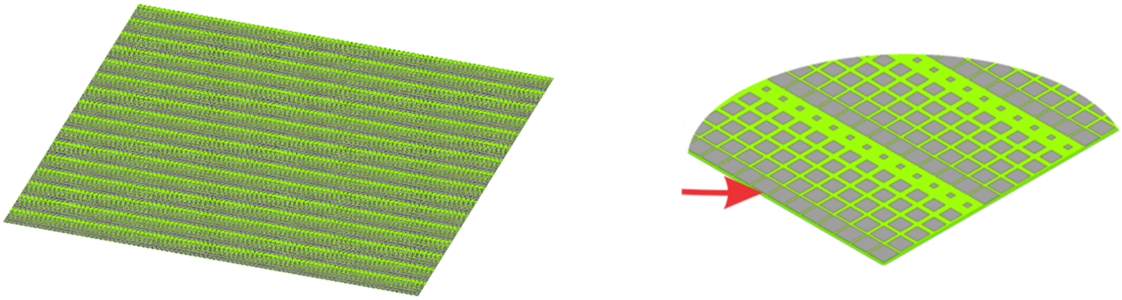

FIGURE 1. Typical passive meta-reflector.

and orientations, allowing optimization of antennas orientation and beam forming codebooks. In [13], a general-purpose model for scattering from finite-size metasurfaces was embedded in a 3D ray-tracing simulator and applied to indoor scenario. In that work, similar to many others, the near-field nature of the scattering was not considered which limited the size of the reflectors for which such coverage models are applicable. In [14], the authors proposed a method for efficient calculation of the scattered electric field taking into account the mutual coupling of unit cells. In [15], the approach for cross-polarization modeling of the reflector-antennas was proposed with a description of how to apply the Fourier transform for improving the calculation speed.

The goal of the present work is to develop a model, which quantifies the changes of signal propagation quality, when intelligent reflective surfaces are introduced in the indoor environment. The proposed model allows designing the meta reflectors, assessing impact of their size, of the RN beams they operate with, and environment features on the received power coverage.

This paper is organized as follows. In Section 2, we discuss the baseline modelling procedure without finite-area reflectors. In Section 3, we describe how to include a passive reflector on top of the baseline model. In Section 4, we describe one of the components of the passive reflector model, namely the scattering response of the finite reflector and its relation to radar cross-section. In Section 5, we present a semi-analytical model of the reflector radar cross-section. In Sections 6 and 7, we present the outline of the modelling procedure using either analytical or numerical radar cross-section models. Finally, Section 8 presents the experimental validation of the proposed model. In appendix, we provide detailed analytical derivation of the proposed model.

2. IMPACT OF MULTIPATH AND MULTIPLE BEAMS

In evaluating the effects of meta-reflectors, it is often assumed that signals predominantly propagate via the Line-of-Sight (LOS) path, with the Non-Line-of-Sight (NLOS) signal deemed negligible. While it is accurate that the Reference Signal Received Power (RSRP) is commonly determined by a LOS component, it is important to note that even in scenarios where the LOS path is blocked, and no reflectors are present, the received signal power may still be significant. This can occur due to power reaching the receiver via NLOS paths. The existence of these NLOS propagation paths can diminish the perceived impact of reflectors when they are introduced. As a result, calculations that do not consider multipath propagation may often overestimate the impact of meta-reflectors. Another common misconception that leads to the overestimation of meta-reflector's impact is the assumption that a wireless system operates a single beam with one predominant direction of directivity, which determines coverage. This assumption overlooks the fact that commercial Radio Nodes (RNs) operate multiple beams, with beam codebooks designed for omnidirectional coverage.

Multipath reflections, penetrations of the radio signal, separation of the propagation channel, and beamforming are all factors described in stochastic geometrical channel models, such as 3GPP 38.901 [12], implemented in the QuaDRiGa [16] channel model, NYU mmWave [17], among others [18, 19]. These models quantify various parameters for NLOS propagation scenarios, including path losses, shadow fading, and angular spreads of departure and arrival. However, a limitation of stochastic models for meta-reflector studies is that finite-area reflectors can only enhance received power on top of the existing channel contribution.

In certain cases, it is crucial to consider how the finite area-reflector replaces the channel contribution of the existing wall area, characterized by material and slab parameters such as dielectric constant and loss tangent. Deterministic models, such as PyLayers [21–23] and Nvidia Sionna [24], offer an alternative to stochastic modeling, allowing for the modeling of azimuth and elevation angles of departure and arrival, propagation path time delays at each obstacle, and amplitudes and phases of each propagation path, including electromagnetic wave polarization transformations at each obstacle. The downside of deterministic modeling is the difficulty of capturing all minute environmental details, such as the presence of gridded metallic supporters within drywalls, which can significantly influence radio propagation, but whose exact geometry can be unknown.

The advantage of separating antenna impact and propagation channel impact, a feature shared by both stochastic and deterministic models, is that it simplifies the computational complexity of multiple beam simulations. This is achieved by applying beamforming codebooks in post-processing and transferring the impulse response function (IRF) into channel models for link level simulation such as the tapped delay line (TDL) or clustered delay line (CDL) channels.

For each propagation path τ, we define a 2×2 matrix of complex-valued coefficients C_τ, representing environment impact on the signal. Transmitter (Tx) impact is described by the gain values of the two electric field components out of the Tx antenna in the direction of the path $F^{\boldsymbol{\varphi}}_{Tx}$ and $F^{\boldsymbol{\theta}}_{Tx}$. Receiver (Rx) impact is described analogously by the gain components of the Rx antenna $F^{\boldsymbol{\varphi}}_{Rx}$ and $F^{\boldsymbol{\theta}}_{Rx}$. As inspired by [12] Eq. (8.4.27), the IRF at the delay tap τ is given as:

$$IRF_\tau = \begin{bmatrix} F^{\boldsymbol{\theta}}_{Rx} \\ F^{\boldsymbol{\varphi}}_{Rx} \end{bmatrix}^T \cdot \begin{bmatrix} C^{\boldsymbol{\theta\theta}}_\tau & C^{\boldsymbol{\theta\varphi}}_\tau \\ C^{\boldsymbol{\varphi\theta}}_\tau & C^{\boldsymbol{\varphi\varphi}}_\tau \end{bmatrix} \cdot \begin{bmatrix} F^{\boldsymbol{\theta}}_{Tx} \\ F^{\boldsymbol{\varphi}}_{Tx} \end{bmatrix} \tag{1}$$

For a single LOS path channel coefficient is:

$$\mathrm{C}_\tau = \begin{bmatrix} C^{\boldsymbol{\theta\theta}}_\tau & C^{\boldsymbol{\theta\varphi}}_\tau \\ C^{\boldsymbol{\varphi\theta}}_\tau & C^{\boldsymbol{\varphi\varphi}}_\tau \end{bmatrix} = \frac{-j\lambda_0}{4\pi} \frac{e^{-j2\pi d/\lambda_0}}{d} \begin{bmatrix} 1 & 0 \\ 0 & 1 \end{bmatrix}, \tag{2}$$

where d is the distance of propagation, and λ_0 is the carrier wavelength.

3. INCLUSION OF REFLECTORS SCATTERING INTO THE GEOMETRICAL CHANNEL MODEL

To include the finite-area reflective surface in the geometrical channel model, we propose a method illustrated in Fig. 2, where additionally to the original Tx-Rx channel with path coefficient matrices $\mathrm{C}_{\tau_{TR}}$ (where TR refers to **T**x->**R**x paths set), we perform the computation of two additional sets of channel paths: $\mathrm{C}_{\tau_{TS}}$ channel paths (from **T**x to the reflective **S**urface center) and $\mathrm{C}_{\tau_{SR}}$ (channel paths from the **S**urface center to the **R**x).

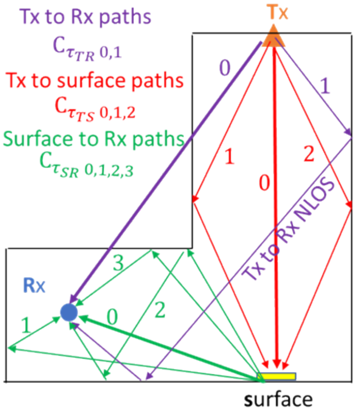

FIGURE 2. Channel paths required in the proposed formalism of finite-area reflectors scattering inclusion into the geometrical channel model.

The channels $\mathrm{C}_{\tau_{TS}}$ and $\mathrm{C}_{\tau_{SR}}$ are combined, by drawing all combinations of paths between these two with the new paths having delays $\tau_{TSR} = \tau_{TS} + \tau_{SR}$, departure angles $\theta_{D_{TS}}$, $\varphi_{D_{TS}}$, and arrival angles $\theta_{A_{SR}}$, $\varphi_{A_{SR}}$. As an example, given three paths from Tx to the reflective surface and four paths from the surface to Rx, the total number of path combinations will be $4 \cdot 3 = 12$. These channels represent propagation paths from Tx to Rx, each path containing exactly one reflection from the considered finite area surface. The coefficients matrices of these channels for each path τ_{TSR} are calculated by a double matrix-product, which extends the transfer matrices product formalism of [25] for metareflectors:

$$\mathrm{C}_{\tau_{TSR}} = \mathrm{C}_{\tau_{SR}} \cdot \mathrm{R}_{D,A} \cdot \mathrm{C}_{\tau_{TS}}, \tag{3}$$

where $\mathrm{C}_{\tau_{TSR}}$ is the newly obtained set of combined channel paths. 'TSR' stands for **T**x-**S**urface-**R**x. The paths are combined by means of a special matrix $\mathrm{R}_{D,A}$, which is determined by the finite area reflector scattering response. Reflector scattering response depends on the angle pair of incidence (arrival) $\theta_{A_{TS}}$, $\varphi_{A_{TS}}$ of the Tx-surface channel path τ_{TS} and specific departure angle pair of scattering $\theta_{D_{SR}}$, $\varphi_{D_{SR}}$ of the surface-receiver channel path τ_{SR}. The analytical expression for $\mathrm{R}_{D,A}$ is provided further. Indexes D and A thus refer simultaneously to a specific paths set (TS or SR), paths index (delay component of the set), and the angle pair type — departure or arrival (D or A) at the reflector center.

One of the components of the final matrix of Eq. (3) is expressed as:

$$\begin{aligned} C^{\boldsymbol{\theta\theta}}_{\tau_{TSR}} &= C^{\boldsymbol{\theta\theta}}_{\tau_{SR}} \cdot R^{\boldsymbol{\theta\theta}}_{D,A} \cdot C^{\boldsymbol{\theta\theta}}_{\tau_{TS}} + C^{\boldsymbol{\theta\varphi}}_{\tau_{SR}} \cdot R^{\boldsymbol{\varphi\theta}}_{D,A} \cdot C^{\boldsymbol{\theta\theta}}_{\tau_{TS}} \\ &\quad + C^{\boldsymbol{\theta\varphi}}_{\tau_{SR}} \cdot R^{\boldsymbol{\varphi\varphi}}_{D,A} \cdot C^{\boldsymbol{\varphi\theta}}_{\tau_{TS}} + C^{\boldsymbol{\theta\theta}}_{\tau_{SR}} \cdot R^{\boldsymbol{\theta\varphi}}_{D,A} \cdot C^{\boldsymbol{\varphi\theta}}_{\tau_{TS}} \end{aligned} \tag{4}$$

R coefficients in Eq. (4) are inspired by [6] Eq. (18) β factor, which in present work is extended for multipath and polarization tracking. Eq. (4) and consequently Eq. (3) can be understood as follows. There are four ways of how field component originating as $\boldsymbol{\theta}$ field at the Tx arrives as $\boldsymbol{\theta}$ field at the Rx. There are four such contributions to the final field in total and three out of four experience intermediate transformation into $\boldsymbol{\varphi}$ component at some point: during interactions within Tx-surface channel, during scattering from the finite-area reflector surface, or during interactions within surface-Rx channel.

4. SCATTERING RESPONSE

For quantifying scattering pattern of the surface, bistatic radar cross-section (RCS) metric σ is applied. RCS is different for each angle of incidence and polarization of the incident wave, and responsible for making many of the path pairs of the $C_{\tau_{TSR}}$ channel insignificant acting as a spatial filter. As we consider separating the scattered electric fields vector components and calculating individual RCS for each component $\mathbf{e}_D$ $\mathbf{e}_A$, we write the elements of $\mathrm{R}_{A,D}$ matrix as (the derivation provided in Appendix D):

$$R^{\mathbf{e}_D,\mathbf{e}_A}_{D,A} = \sqrt{\frac{4\pi}{\lambda_0^2}\sigma^{\mathbf{e}_D,\mathbf{e}_A}_{D,A}}\, e^{+j\beta(d_{TS}+d_{SR})} \tag{5}$$

λ_0 is the wavelength of radio wave, and σ represents the radar cross-section per pair of the incident electric field vector component $\mathbf{e}_A$ and scattered electric field vector component $\mathbf{e}_D$. The pairs $\mathbf{e}_D$, $\mathbf{e}_A$ represent one of the four possible polarization component pairs: $\boldsymbol{\theta}_D\boldsymbol{\theta}_A$, $\boldsymbol{\theta}_D\boldsymbol{\varphi}_A$, $\boldsymbol{\varphi}_D\boldsymbol{\theta}_A$, or $\boldsymbol{\varphi}_D\boldsymbol{\varphi}_A$. The RCS in Eq. (5) can be defined as:

$$\sigma^{\mathbf{e}_D,\mathbf{e}_A}_{D,A}[m^2] = \lim_{r\to\infty}\left[4\pi r^2 \frac{\|\mathbf{E}^{\mathbf{e}_D,\mathbf{e}_A}_D\|^2}{\|\mathbf{E}^{\mathbf{e}_A}_A\|^2}\right], \tag{6}$$

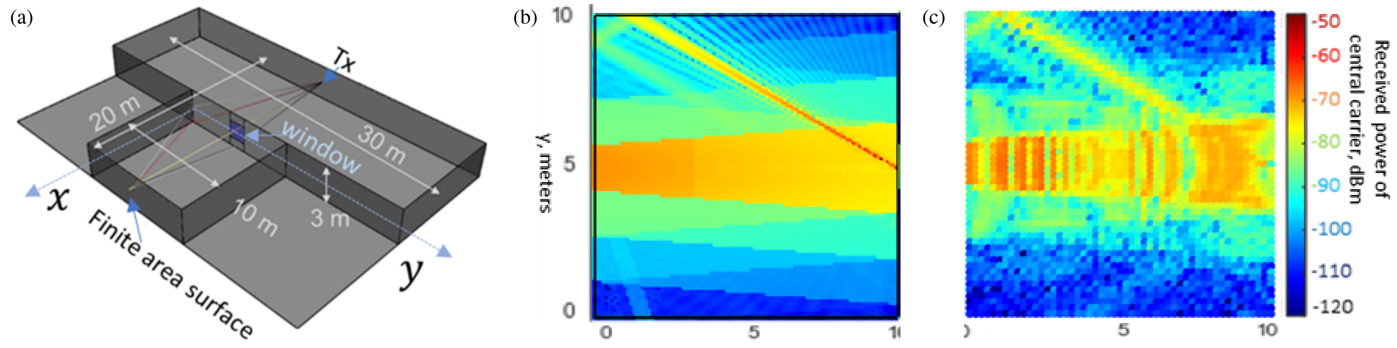

Artificial layout

Geometrical model

HFSS SBR

FIGURE 3. Test layout for cross-check of the geometrical model in presence of finite surface scattering. (a) Proposed geometrical model extension. (b) HFSS shoot and bounce method [27].

where the definition of RCS from [26] is applied to individual field polarization components of the incident $\boldsymbol{e}_A$ and scattered $\boldsymbol{e}_D$ electric fields as opposed to the total electric field.

Each component of the incident electric field $E_A^{\mathbf{e}_A}$ corresponds to the direction of arrival θ_A, φ_A of the channel from Tx to the surface. Each scattered field component $E_D^{\mathbf{e}_D}$ corresponds to the direction of departure θ_D, φ_D of the channel from the surface to Rx. The relationships between the field components and angles of departure or arrival in spherical coordinates are:

$$\boldsymbol{\theta}_\tau = \begin{bmatrix} \cos\theta_\tau \cos\varphi_\tau \\ \cos\theta_\tau \sin\varphi_\tau \\ -\sin\varphi_\tau \end{bmatrix} \quad \boldsymbol{\varphi}_\tau = \begin{bmatrix} -\sin\varphi_\tau \\ \cos\varphi_\tau \\ 0 \end{bmatrix} \quad \mathbf{s}_\tau = \begin{bmatrix} \sin\theta_\tau \cos\varphi_\tau \\ \sin\theta_\tau \sin\varphi_\tau \\ \cos\theta_\tau \end{bmatrix} \tag{7}$$

The resulting set of paths, which is used for defining IRF, is a concatenation (or merging) of Tx-Rx paths and Tx-surface-Rx paths. The paths from original Tx-Rx channel, which propagate through the surface of reflector (i.e., reflect from the wall behind the reflector) must be removed (filtered out) before concatenation.

$$\mathrm{C}_{final} = \mathrm{C}_{TR}^{filtered} \cup_\tau \mathrm{C}_{TCR}, \tag{8}$$

where $\cup_\tau$ is the union operation over the two sets of paths. i.e., if the first set has 2 paths and the second set 12 paths, the final set will have 14 paths. All delay components C_τ of the set C_{final} in Eq. (8) can be inserted back into Eq. (1) for impulse response calculations.

To illustrate the modeling approach, we designed an artificial indoor layout example shown in Fig. 3(a). This layout includes an isolated room, which receives a boresight beam from Tx antenna installed at the wall outside the room. The beam enters isolated room through a 1.5×1.5 meters window and hits a 0.3×0.3 meters meta-reflector (as shown in Fig. 1) at the opposite wall of the isolated room. Meta-reflector tilts the scattered beam by 30 degrees of azimuth. Side walls at the Tx side area are spread apart from TX, helping to reduce the impact of reflections from these walls on the coverage map. As one of the validations of the proposed method, Figs. 3(b)–(c) show the comparison of the described geometrical model against Ansys High Frequency Simulation Software (HFSS) [27] ray shooting and bouncing simulation, using a rotated metal plate as a finite-area scatterer. RN uses the 4×8 antenna array radiation pattern with 41 dBm EIRP and approximately 15 degrees beamwidth. For the walls we chose an arbitrary brick material with 5 cm thickness, relative permittivity of 4, and loss tangent of 0.05. For the floor and ceiling we assumed concrete material with permittivity of 8.7, loss tangent of 0.22, and thickness of 10 cm. The carrier frequency was 28 GHz. The HFSS simulation assumed narrow-band continuous-wave signal, resulting in high and low received power variation along the propagation direction. In the geometrical channel model, the signal is assumed wideband, and the powers of individual propagation paths were added incoherently. HFSS simulation took 100 times longer than the developed model, and simulation time ratio would scale if system operates multiple beams.

5. SEMI-ANALYTICAL MODEL OF THE FINITE REFLECTIVE SURFACE RADAR CROSS-SECTION

For the semi-analytical modeling of the RCS, we propose the following expression which extends the formalism in [6] Eqs. (19), (22):

$$\sigma_{D,A}^{\mathbf{e}_D,\mathbf{e}_A} = 4\pi \left(\frac{a_c^2}{\lambda_0} \right)^2 \cdot G_{D,A}^{\mathbf{e}_A} \cdot e_{D,A}^{\mathbf{e}_D,\mathbf{e}_A} \tag{9}$$

Note that the definition of Eq. (6) can be used to extract RCS data from electromagnetic simulations, while analytical expression of Eq. (9) is derived from Eq. (6), with derivation provided in Appendix C. a_c is the size of the unit cell, which is assumed equal for all unit cells and equal to inter-cell spacing. λ_0 is the wavelength of radio wave. The angular-dependent array factor is

$$G_{D,A}^{\mathbf{e}_A} = \left| \sum_{c=1}^{N_c} \psi_{D,c} \cdot w_c^{\mathbf{e}_A} \cdot \psi_{A,c} \right|^2 \tag{10}$$

$\psi_{A,c}$ is the incident wavefront phase factor of the Tx-surface path A at the reflective surface unit cell location c. $\psi_{D,c}$, analogously, is a phase-factor with phase offset of the surface-Rx path D at the unit cell location c. N_c is the total number of unit cells in the reflector surface plane. In the far field, the phase factors are:

$$\psi_{A,c} = e^{-j\frac{2\pi}{\lambda_0}\mathrm{c}\cdot\mathrm{s}_A} \quad \psi_{D,c} = e^{-j\frac{2\pi}{\lambda_0}\mathrm{c}\cdot\mathrm{s}_D} \tag{11}$$

s_A represents the direction vector of arrival of the path A of the Tx-surface channel, according to definition of the vector in Eq. (7). s_D is the direction vector of the departure path D of the surface to Rx channel. c is the unit cell location vector. In the reviewed literature, the Tx-surface phase term often has the opposite sign, but in the present work, both phase terms have the same negative exponents. This is because we follow a convention, where the Tx-reflector incident wave vector is directed towards the surface, and the angles of arrival are defined accordingly, as opposed to defining angles in the direction to Tx.

5.1. Concept of Local Phase Response

w_c includes the phase offset introduced by the metasurface unit cell on the incident plane wave upon reflection. Semi-analytical model assumes that each unit cell of the surface reflects with its own phase shift in w_c which is unique for each unit cell type and incident field polarization e_A, however does not depend on the types of the surrounding unit cells and the angle of incidence, thus does not consider mutual coupling. The techniques similar to the one described in [14] can be applied however in this model for mutual coupling inclusion.

For a most basic metasurface, which imposes anomalous direction of reflection, the phase offset may compensate the phase differences of the strongest Tx-surface and surface-Rx path pairs for some target Rx direction:

$$w_c = \mathrm{conj}(\psi_{c,A=\mathrm{argmax}(|C_{TS}|)} \cdot \psi_{c,D=\mathrm{argmax}(|C_{SR}^{target}|)}) \tag{12}$$

$A = \mathrm{argmax}(|C_{TS}|)$ represents the path index with minimum propagation loss within the paths between the Tx and the surface. $D = \mathrm{argmax}(|C_{SR}^{target}|)$ finds the path index with minimal losses within the paths between the surface and the target Rx. conj performs compensation of the found path phase at the unit cell location c to provide peak of the scattering in the direction to the target Rx.

The values of w_c may slightly vary for a unit cell at different angles of incidence and incident field polarization, and be obtained from electromagnetic simulations for each unit cell type by applying periodic boundary conditions. Alternatively, some analytics exist [28] to predict unit cell phases given the geometry of the cells, although such may be inaccurate or complicated if the consideration of mutual-coupling effects is required.

Justification of w_c physical meaning is provided in Appendix E.

5.2. Field Vector Projection Term

The last factor in RCS semi-analytical expression of Eq. (9) follows physical optics assumption for the electric current density in the reflective surface plane. n represents the surface normal orientation vector.

$$e_{A,D}^{\mathbf{e}_D,\mathbf{e}_A} = |\mathbf{e}_D \cdot [\mathbf{n} \times (\mathbf{s}_A \times \mathbf{e}_A)]|^2 \tag{13}$$

Note that in the analytical model, Tx-surface and surface-Rx rays need to be filtered based on the signs of vectors dot products $\mathbf{s}_D \cdot \mathbf{n}$ and $\mathbf{s}_D \cdot \mathbf{n}$ expressions correspondingly. If the sign of either is negative, it means that rays incident on the back of the reflector will contribute to scattering, or rays generated by currents in infinitely flat reflector and propagating backwards will be included.

To illustrate the impact of the polarization-dependent factor on the Tx-surface-Rx channel gain component, we performed modeling in MEEP [29] of the 8.5×8.5 cm surface designed to reflect a boresight incident wave at $\theta_D = 45°, \phi_D = 0°$. Surface normal vector was oriented in z direction, and unit cells vary in the x direction. Each supercell of the structure was 6 unit cells with phases -120, -60, 0, 60, 120, 180 degrees as shown in Fig. 5.

For electromagnetic simulation, the surface elements were 18 μm thickness perfect electric conductors (PEC) on top of the low loss dielectric with relative permittivity of 4.6. The conductor widths were 1.13, 1.68, 1.82, 1.92, 2.06, and 2.43 mm, and were used to assign the amplitude coefficients according to the conductor areas. Below the dielectric another PEC layer was present. The dielectric losses were ignored. The simulation and modeling results are shown in Fig. 4(a) for $\boldsymbol{\phi\phi}$ (co-polarized) and in Fig. 4(b) $\boldsymbol{\theta\phi}$ (cross-polarized) field components. In the case of incidence at $\theta_A = 0°$, $\phi_A = 0°$, the power happens to scatter mostly into the cross-polarized $\theta\phi$ component of the scattered field — this is purely geometrical effect due to the choice of the polarization basis and has no special physical cause. The results presented in Fig. 4 allow to confirm that the field polarization transformations are correctly captured in the proposed analytical model. The total scattered field peak magnitudes as computed by combining corresponding entries from 4(a) and 4(b) as $\sigma_{Total} = \sqrt{\sigma_{\theta\theta}^2 + \sigma_{\theta\phi}^2}$ have error less than 1 dB.

5.3. Near Field Wavefront Sphericity

As we found, the inclusion of near-field effects has detrimental impact for indoor scenarios modeling. The far-field approximation can be applied only when the $d > 2\frac{L^2}{\lambda_0}$ inequality holds. Here, d is the distance between the reflector and the Rx, and L is the largest side length of the reflector. For 8×8 antenna arrays spaced at the half wavelength spacing the plane wave approximation starts at the $2(0.01/2 \cdot 8)^2/0.01 = 0.32$ meters distance, which is short enough to consider all indoor coverage points to be far field for such an antenna array. For 30 cm reflective surface at 28 GHz however, the far field starts only after $2 \cdot 0.3^2/0.01 = 18$ meters of propagation which does not suit indoor short distance propagation modeling. When radiative near-field Fresnel propagation model is used instead, i.e., spherical-wave approach, the applicability inequality becomes $d > 0.62\sqrt{\frac{L^3}{\lambda_0}}$. Given this expression, for a half meter surface the minimal modeling distance becomes $0.62\sqrt{0.3^3/0.01} = 1$ meter, which is a lot more suitable for the problem. Such spherical waves model can be included by substituting corresponding expressions of $\psi_{A,c}$ and/or $\psi_{D,c}$ by formulas containing the exact distances from Tx/Rx to the corresponding unit cell center

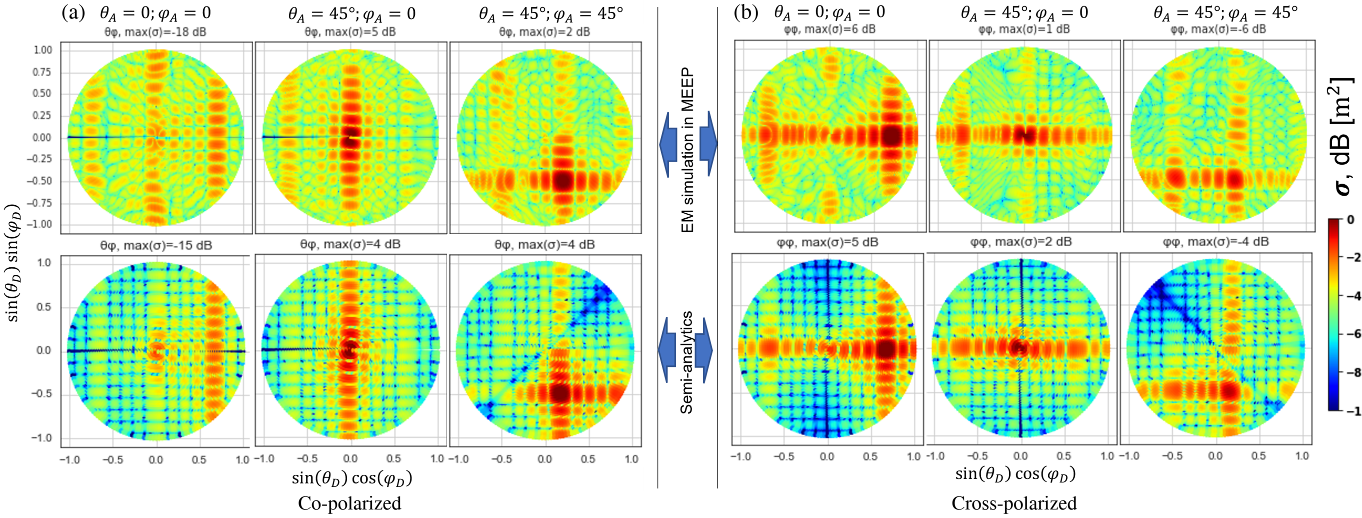

FIGURE 4. RCS angular patterns of $\phi\phi$ field components, obtained using electromagnetic simulations in MEEP software (top) and modeling results based on proposed semi-analytical model (bottom) for different directions of incident plane wave $\theta_A, \phi_A, =$ (a) $(0^{\circ}, 0^{\circ})$, (b) $(45^{\circ}, 0^{\circ})$, (c) $(45^{\circ}, 45^{\circ})$.

TABLE 1. Ways to include incident beam amplitude variation over the surface.

Option	Rescale Tx-Surface-Rx path	Apply amplitude weights at unit cells	Split reflector into sub-parts
Accuracy	Average accuracy: RCS pattern does not depend on the shape of the beam, only on total power	High accuracy: RCS pattern depends on the shape of the incident beam	Accuracy depends on number of reflector parts and post-processing
Computational complexity — separation of antenna and propagation channel impact	Low complexity — rescaling is done after RCS calculation, but each beam needs individual paths rescaling	High complexity — rescaling is done during RCS calculation and each beam needs to be rescaled separately	Low complexity — no paths rescaling required, however number of paths is large
Formula	$\mathrm{C}_{\tau} = \mathrm{C'}_{\tau} \cdot \frac{d_{TS}}{d_{Tx,c}} \sqrt{\frac{\sum_{c=1}^{N_c} G_{Tx,c}}{N_c G_{TS}}}$	$w'_c = w_c \frac{\sqrt{G_{Tx,c}} d_{TS}}{\sqrt{G_{TS}} d_{Tx,c}}$	$\mathrm{C} = \mathrm{C}_{TR}^{filtered} \cup_{\tau} \mathrm{C}_{TSR_1} \cup_{\tau} \mathrm{C}_{TSR_2} \ldots$

location:

$$\psi_{A,c} = e^{-j\frac{2\pi}{\lambda_0} d_{A,c}}, \quad \psi_{D,c} = e^{-j\frac{2\pi}{\lambda_0} d_{D,c}} \tag{14}$$

$d_{A,c}$ is the Tx-surface path A total propagation distance from the Tx to the unit-cell c. Correspondingly, $d_{D,c}$ is the total propagation distance of the path D from the unit cell c to the Rx. Long-distance propagating paths may be calculated using the far-field propagation path model of Eq. (11), whereas short-distance propagating paths must consider exact distances to unit cell locations as in Eq. (14).

The usage of near-field model for surface-Rx phase terms allows to avoid overestimation of the beam power and underestimation of the beamwidth at the receiver points close to the reflector surface. Near-field inclusion for Tx-surface phase term allows to capture beam spreading illustrated in Fig. 6, as naturally included in geometrical optics (GO), but does not occur with plane-wave scattering as derived in physical optics (PO) formalism. The expected beam spreading after reflection from a square reflector for normal incidence can be estimated by $\Delta\varphi = 2 \cdot \mathrm{atan}(L/2/d_{TS})$.

5.4. Incident Beam Amplitude Variation

In Eqs. (3) and (10), it is assumed that reflector is illuminated by the same directivity value of the incident beam at each point of the reflector as calculated at the central point of the reflector. In near field, the incident beam amplitude variation of the narrow RN beams starts playing a role: unless beam amplitude variation over the reflector surface is included, the coverage gain may become overestimated. There are three ways to include such variation in modeling, outlined in Table 1.

5.5. Diffraction Grating Effect

In cases that meta reflector is a periodic structure and does not consider techniques of removing structure periodicity [30], additional diffraction lobes will be present. Those appear because

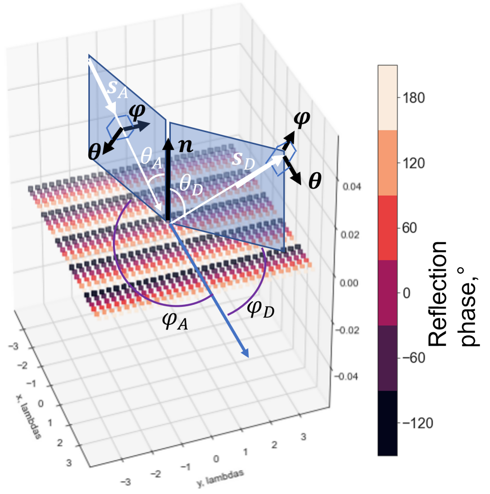

FIGURE 5. Illustration of the meta reflector, used for cross-check between the semi-analytical model and electromagnetic model of RCS.

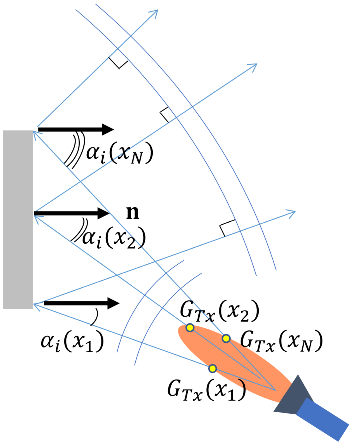

FIGURE 6. Illustration of near-field effects. Beam widening after reflection is included only by spherical waves consideration. Effective size of the reflector is determined by the beam width out of the Tx antenna.

of the diffraction-grating effect, coming from the periodicity of the super cells over the surface, where each supercell is composed of several unit cells. Diffraction grating equation is given by:

$$i \cdot a_c(\sin\theta_{scat} + \sin\theta_{inc}) = m\lambda_0 \tag{15}$$

In this formula, $i \cdot a_c$ is the periodicity of the super cell, θ_{inc} the angle of incidence, θ_{scat} the angle of scattering, and m integer. For example, for a metasurface consisting of 6-element supercells, with unit cells spaced at $\lambda_0/3$, $\sin\theta_{scat} = m\lambda_0/(\lambda_0/3 \cdot 6)$, and the peaks from diffraction grating are expected at $\theta_{scat} = \arcsin m/2 = 0°, \pm 30°, \pm 90°$ with $m = 0, \pm 1, \pm 2$ correspondingly.

To account for diffracting lobes in the proposed semi-analytical model, as an alternative to the Floquet harmonics representation [31], we propose specifying individual amplitude weights of the surface unit cells via w_c factor. Such amplitude weights approach might be more convenient as it avoids the introduction of additional rays into the model. The amplitude weights of w_c are assigned according to the areas of unit cells conductor elements and normalized such that $\sum_{c=1}^{N_c} |w_c|^2/N_c = 1$. Fig. 7 shows the impact of amplitude weights inclusion in the model and comparison to electromagnetic simulation and Floquet modes approach where the amplitudes of the Floquet modes are fitted from simulations, for a 30 × 30 cm meta-reflector. It is important to note that we do not expect amplitude coefficient model works well for any types of unit cells, although in present work in Fig. 4 we successfully applied such approach to surfaces with square-shaped conductor elements. From Fig. 7 it can be observed that Floquet modes model allows capturing diffraction lobes powers more accurately compared to the amplitude weights model. Single scattered wave approach does not predict any diffraction grating lobes.

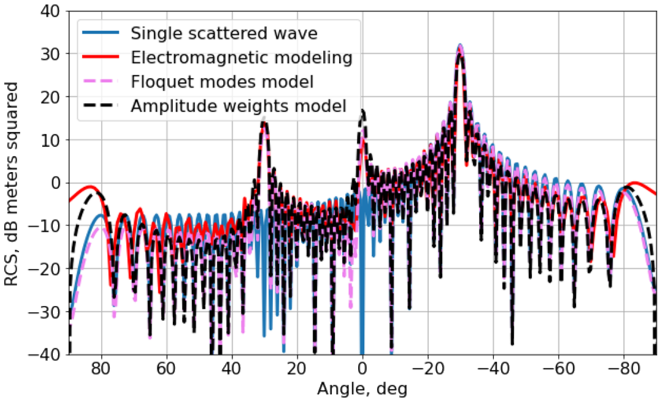

FIGURE 7. Result of the amplitude weights inclusion to capture diffraction lobes due to periodic structure of the surface. RCS azimuth cut for $\boldsymbol{\theta\theta}$ field incident onto surface facing z axis.

It needs to be summarized that w_c may include following factors:

1. unit-cell phase response
2. unit-cell amplitude response (efficiency)
3. incident beam amplitude at the unit cell

6. MODELING ALGORITHM OUTLINE

The overall modeling procedure can be outlined in the following steps:

1. Calculate a multipath channel — complex coefficients, delays, and angles of arrival and departure — between Tx and Rx isotropic antennas, for all four possible combinations of input/output field vector orientations.
2. Filter paths which propagate through the area of the reflector. For example, some original paths may reflect from (or penetrate through) the wall where finite reflective surface is installed.
3. Calculate two additional multipath channels: from Tx to the reflecting surface central point, and from reflecting surface central point to the Rx.

TABLE 2. Advantages and disadvantages of the RCS models.

Feature/Approach	Electromagnetic simulation	Semi-analytical model
EM simulations complexity	High	Low
Reuse of EM data for other source Tx locations and patterns, other reflector sizes and phase designs	No	Yes
Unit cells phase optimization	Slow	Fast
Scattering pattern representation accuracy	High	Low

4. For each combination of Tx-surface and surface-Rx paths, apply reflector response to obtain a combined Tx-surface-Rx path.
5. Merge the filtered Tx-Rx channel from step 2 with the Tx-surface-Rx channel paths from step 4, according to Eq. (8).
6. Apply spatial filtering at the Tx and Rx antennas according to the antenna radiation patterns and beamforming codewords.
7. Calculate received power or pass spatially filtered coefficient-delay profiles to link level simulations as tapped delay line channels or non-filtered coefficient-delay-angular profiles as clustered delay line channels.

7. NUMERICAL VS ANALYTICAL MODELING OF INTELLIGENT REFLECTORS

There are two options of obtaining the RCS of the surface

(a) Electromagnetic modeling of RCS.

   (1) From geometrical channel modeling extract incidence and scattering angle pairs of all path combinations of the Tx-surface and the surface-Rx channels.
   (2) Pass these angles to the electromagnetic model as the directions of incidence and scattering.
   (3) Set up whole reflector in EM modeling with explicit source beam (not plane wave).
   (4) Calculate RCS for all pairs of input-output polarization components.
   (5) Pass the obtained RCS values back into geometrical model

(b) Semi-analytical model of RCS.

   (1) For each unique unit cell type, set up an EM model assuming that the unit cell is repeated infinitely over the surface.
   (2) Calculate phase and amplitude responses of the unit cell for two orientations of the normal-incident plane wave.
   (3) Pass the obtained local phase response data into the geometrical channel model.

Advantages and disadvantages of each approach are summarized in Table 2. To account for mutual coupling in the semi-analytical model, the phase shifts of unit cells must be obtained considering the neighboring unit cells via local phase response technique. Existing semi-analytical diffracting lobes models are applicable to only limited types of unit cells configuration and relatively large surfaces.

8. EXPERIMENTAL VALIDATION

In this section, we present results for experimental measurements. The measurements setup is illustrated in Fig. 8. The used equipment included a 5G 28GHz Radio Node — SCRN-520-28 which operated multiple beams, together with a 5G Centralized Unit (CU) — Service Node (SN), as well as Aricent Evolved Packet Core (EPC) for Control layer and Separate Data Plane Development Kit (DPDK). The Reference Signal Received Power (RSRP) was measured by means of the walking tests with a Samsung Galaxy S20 5G UW UE hardware with a customized sim-card and G-NetTrack Pro software. For reflector, a 1 × 1 meters metal plate on a wooden rig was used to represent a metasurface. Center of the plate was at the cubicle wall height level of 1.6 m, and linear phase gradient was emulated by a specific tilt angle of the plate, targeting one of the RN beams redirection into the direction parallel to floor. We considered three installation locations of a ceiling-mounted RN over the typical office area, as shown in Fig. 9(a): the RN was either in the center of area A (location 1), in the bottom of the area (location 2), or in the right of the area (location 3). For central installation of the radio node, location of the reflector in-

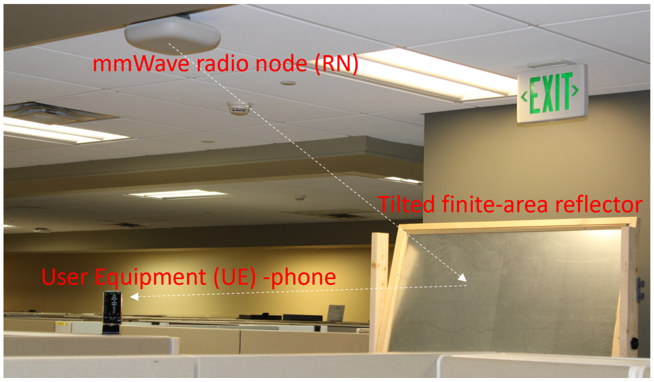

FIGURE 8. A photo of experimental setup.

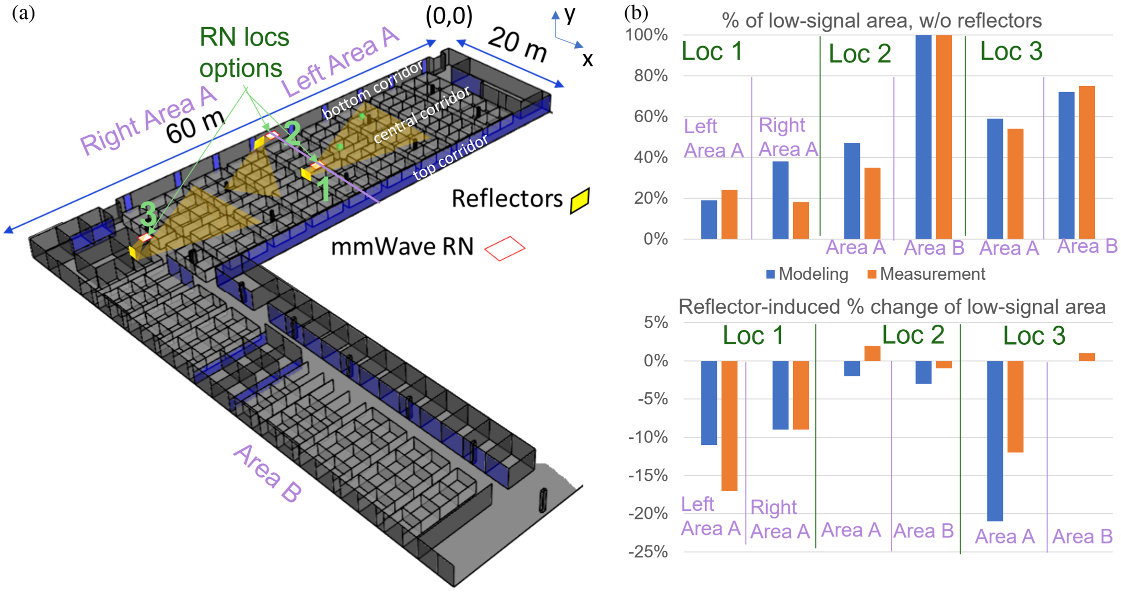

FIGURE 9. (a) Office area for received power measurements and proposed model validation. (b) Obtained statistics of power coverage.

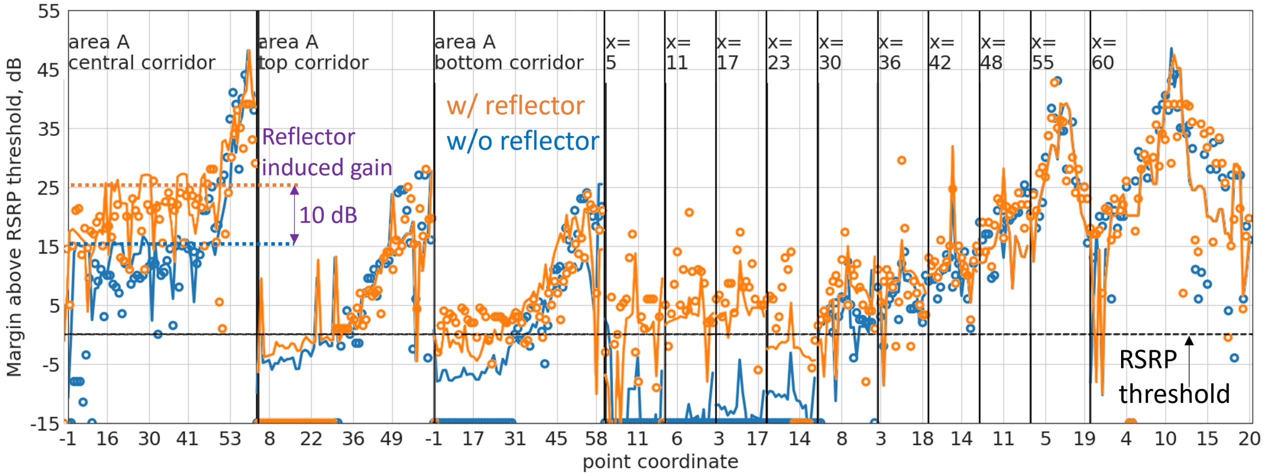

FIGURE 10. Example of measured and modelled received power, for right RN installation option (location 3) and area A. Circles are for measurements, lines — modeling.

stallation was different for the left and right areas, either from the right or from the left of the RN, to provide gain in the left or right areas correspondingly. The system was simulated using PyLayers ray tracing model with incorporated model of the passive reflectors as described in the present paper and phased-array models of RN and UE antennas, which included the beamforming codebooks and antenna element gain patterns. Across different measurements, the difference between simulated and measured results was found to be on average 4 dB of RSRP. No-signal area percentage estimation difference was calculated to be on average 7.5%, as determined by the CDF point at no signal level. When power level dropped below the sensitivity threshold, the actual power became unknown and was arbitrarily assigned a value of −15 dB relative to the RSRP threshold. Absolute measurement minus modeling differences of the reflector impact were found to be on average 1.5 dB, and 3.7% at the RSRP threshold. Despite that there are no specific metasurface measurements presented in this validation, we still consider the presented results applicable to confirm accuracy of the meta-reflector model incorporation into the geometrical channel model, while the features of the meta-reflector compared to the solid metal plate are validated separately against EM simulations presented in the previous sections. As can be observed from Figs. 9(b), 10, and 11(b), the impact of reflector on the received power is captured both qualitatively and quantitatively correctly by the proposed model. For example, for RN installations at locations 1 and 3, both model and measurements show around 10 dB reflector-induced RSRP gain along the main corridor of area A; the shape of the scattered beam reflected from the reflector has similar azimuthal spreading after reflection;

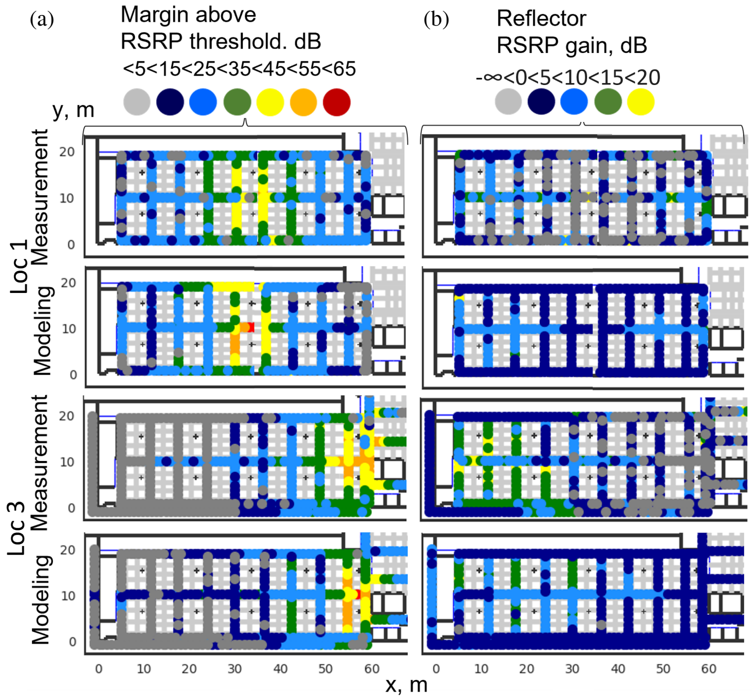

FIGURE 11. (a) Baseline (no reflectors) RSRP above no-coverage threshold level. (b) RSRP gain due to passive reflector over the baseline.

and the percentage of the area where coverage is below threshold decreases with the help of reflectors by 10%. For RN installation at location 2, both model and measurements show no gain due to reflector.

9. CONCLUSIONS

We developed a geometrical channel model capable of predicting the impact of the finite-area reflective surfaces, such as passive meta reflectors, on the received power coverage in indoor environments. The model unifies semi-analytical and electromagnetic approaches for reflective surfaces scattering patterns. Model is validated against HFSS shooting and bouncing simulation and experimental measurements of the received power for a mobile phone and commercial mmWave radio node for the metal plate. We also developed a semi-analytical model of the metasurface scattering pattern, to aid metasurface design and optimization from the system level perspective. The proposed semi-analytical model incorporates many of the existing efforts of semi-analytical finite area reflectors modeling approaches and considers multiple subtleties, such as spherical waves, multipath, dual polarization, and alternative way of diffraction grating effect inclusion. The model is fully compatible with the state of the art three-dimensional dual-polarization geometrical channel models where the complex amplitudes, delays, angles of departure and arrival are tracked for beamforming studies and link level simulations. The model is validated against finite difference time domain electromagnetic simulations in MEEP software.

ACKNOWLEDGEMENT

Authors would like to acknowledge Andrey Kobyakov for helping in the review of the polarization-dependent factor, Benjamin Imanilov for proposing the 'room with window' test layout, Aramais Zakharian for providing meta surface design for electromagnetic validations, Anthony Ng'Oma for organizing measurements campaign, Solomon Abraha for deciding the locations of RNs for experimental validation, Dave Castellana for measuring the office area layout for consequent radio measurements and Evgeniy Pustovalov for suggested edits to the paper.

APPENDIX A. ABBREVIATIONS AND SYMBOLS USED IN THE DERIVATIONS

$\times$ denotes vector cross product

$\int_{A_{refl}} \ldots da$ denotes integration over the surface

$\mathbf{A}$ — magnetic field vector potential $[Tm]$

a — area element $[m^2]$

$A_{refl} = a_c^2 N_c$ — total area of the reflector for scattering calculations $[m^2]$

A_{Rx} — effective area of Rx antenna $[m^2]$

$d_{A,c}$ — total propagation distance from Tx to a point in the reflector plane, or unit cell $[m]$

d_{TS} — total propagation distance from Tx to the reflector center $[m]$

$d_{D,c}$ — total propagation distance from reflector point (or unit cell) to the Rx $[m]$

d_{SR} — total propagation distance from reflector center to the Rx $[m]$

e_s — normalized projection of the scattered electric field vector on the evaluated component of that vector

$\mathbf{E}_i$ — electric field vector $[V/m]$ incident on a reflector in reflector plane

E_i — component of the incident electric field vector (θ or φ)

$\mathbf{e}_i$ — normalized orientation vector of the electric field in the reflector plane, defined by $\mathbf{E}_i = E_i\mathbf{e}_i$

$\mathbf{E}_s^{total}$ — scattered electric field vector $[V/m]$

$E_s^{component}$ — component projection of the scattered electric field vector $[V/m]$

$\mathbf{e}_s$ — normalized orientation vector of the evaluated scattered electric field component (θ or φ)

G — array factor of the reflector - the abs square integral or sum of complex exponents over the surface [linear gain]

G_{Tx} — Tx antenna gain in the direction of the path incident upon finite-area reflector [linear gain]

G_{Rx} — Rx antenna gain in the direction of the path coming from finite-area reflector [linear gain]

$\mathbf{H}_i$ — incident magnetic field at the reflector plane. $[A/m]$

$\mathbf{H}_r$ — reflected magnetic field at the reflector plane. $[A/m]$

$\mathbf{J}(x_c, y_c, z_c)$ — current density, generated in the unit cell due to incident magnetic field, $[A/m^2]$

$\mathbf{j}$ — time-independent unitary orientation vector of the current

j — imaginary unit of a complex number

N_c — number of unit cells

$\mathbf{n}$ — unitary orientation vector of the reflector normal in the direction from reflecting surface side.

P_{Tx} — Power out of the Tx antenna $[W]$

P_{Rx} — Received power [W]

$\mathbf{s}_i = \frac{\mathbf{E}_i\times\mathbf{H}_i}{|\mathbf{E}_i||\mathbf{H}_i|} = \frac{\mathbf{k}}{2\pi\lambda_0}$ — orientation unit vector of propagation direction of the incident wave.

$\mathbf{S}_i$ — Poynting vector $[W/m^2]$

S_i — power spectral density of the field incident upon reflector $[W/m^2]$

S_s — power spectral density of the field scattered from reflector $[W/m^2]$

x_c, y_c, z_c — unit cell location, $[m]$

$\eta_0 = \mu_0 c = 120\pi$ — free space impedance $[Ohm]$.

μ_0 — permeability constant of vacuum $[H/m]$

c — speed of light $[m/s]$

$\beta_0 = \frac{2\pi}{\lambda_0}$ — wavenumber $[rad]$

$\omega_0 = \frac{2\pi c}{\lambda_0}$ — angular frequency $[rad/s]$

λ_0 — electromagnetic wave carrier wavelength in vacuum $[m]$

θ — component basis vector of the field, TE-mode

φ — component basis vector of the field, TM-mode

θ_i, φ_i — zenith and azimuth angles of incidence on the reflector

θ_s, φ_s — zenith and azimuth angles of scattering from the reflector

$\psi_{A,c} = e^{-j\beta_0 d_{A,c}}$ — phase factor of the field propagating from Tx to reflector

$\psi_{D,c} = e^{-j\beta_0 d_{D,c}}$ — phase factor of the scattered field propagated from reflector to Rx

APPENDIX B. DERIVATION OF THE ANALYTICAL SCATTERED FIELD EXPRESSION

First, we write down the electric field potential from [26], Eq. (6.96a):

$$\mathbf{A} = \frac{\mu_0}{4\pi}\iint_{A_{refl}} \mathbf{J}(x_c, y_c, z_c)\frac{e^{-j\beta_0 d_{D,c}}}{d_{SR}}da \tag{B1}$$

Then, we write the expression for current density, according to [26], Example 6.5 and Eq. (11.26).

$$\mathbf{J}(x_c, y_c, z_c) = \mathbf{n}\times(\mathbf{H}_i + \mathbf{H}_r) = 2\mathbf{n}\times\mathbf{H}_i \tag{B2}$$

Next, we assume that the orientation and amplitude of the magnetic field vector $\mathbf{H}_i$ incident on the surface is approximately same over the surface plane. Assumption of the uniform amplitude is later removed. The phase of the incident field defined according to exact propagation distance from Tx to the unit cell c is extracted from $\mathbf{H}_i$. Inserting (B2) into (B1), and extracting surface-location independent terms out of the integral, gives:

$$\mathbf{A} = \frac{\mu_0}{4\pi d_{SR}}2\mathbf{n}\times\mathbf{H}_i\iint_{A_{refl}}\psi_{D,c}\psi_{A,c}da \tag{B3}$$

Expressing scattered field at the next obstacle or at the receiver, after the surface, using frequency domain expression from [26] (6.101a) and the far-field approximation of $\mathbf{E}_s$ dependence on A, we write:

$$\mathbf{E}_s^{total} = -j\omega_0\mathbf{A} \tag{B4}$$

To express scattered electric field in terms of incident electric field, we write the relation:

$$\mathbf{H}_i = \frac{1}{\eta_0}\mathbf{s}_i\times\mathbf{E}_i \tag{B5}$$

Inserting (B5) into (B3), and then (B3) into (B4) results in:

$$\boldsymbol{E}_s^{total} = -j\omega_0\cdot\frac{\mu_0}{4\pi d_{SR}}\frac{1}{\eta_0}\cdot 2\boldsymbol{n}\times(\boldsymbol{s}_i\times\boldsymbol{E}_i)\iint_{A_{refl}}\psi_{D,c}\psi_{A,c}da \tag{B6}$$

Using definitions for ω_0 and η_0 and simplifying:

$$\boldsymbol{E}_s^{total} = -j\frac{1}{d_{SR}}\frac{1}{\lambda_0}\cdot\boldsymbol{n}\times(\boldsymbol{s}_i\times\boldsymbol{E}_i)\iint_{A_{refl}}\psi_{D,c}\psi_{A,c}da \tag{B7}$$

We may express scattering field in terms of normalized incident field orientation vector $\mathbf{e}_i$ and phase-independent field amplitude E_i. Also, considering that total scattered field vector can be arbitrarily oriented, for geometrical channel modeling we need to calculate a specific projection (or component) of this field onto θ vector or φ vector. Without defining such vectors at this point, we may write an expression for a component projection of the scattered field as a dot product of the component orientation unit-vector $\mathbf{e}_s$ and total scattered field orientation vector:

$$E_s^{\mathbf{e}_s,\mathbf{e}_i} = \frac{-jE_i}{\lambda_0 d_{SR}}\cdot\mathbf{e}_s\cdot(\mathbf{n}\times(\mathbf{s}_i\times\mathbf{e}_i))\iint_{A_{refl}}\psi_{D,c}\psi_{A,c}da \tag{B8}$$

APPENDIX C. DERIVATION OF ANALYTICAL RADAR CROSS-SECTION

Inserting the scattered field expression of (B8) into (6):

$$\sigma_{D,A}^{\mathbf{e}_D,\mathbf{e}_A} = 4\pi d_{SR}^2 \frac{|E_s^{\mathbf{e}_s,\mathbf{e}_i}|^2}{|E_i^{\mathbf{e}_i}|^2} \tag{C1}$$

Introducing scalar terms e_s and G

$$e^s = |\mathbf{e}_s \cdot (\mathbf{n} \times (\mathbf{s}_i \times \mathbf{e}_i))|^2 \tag{C2}$$

$$G = \left| \frac{1}{A_{refl}} \iint_{A_{refl}} \psi_{D,c}\psi_{A,c} da \right|^2 \tag{C3}$$

$$\sigma_{D,A}^{\mathbf{e}_D,\mathbf{e}_A} = 4\pi d_{SR}^2 \frac{\frac{1}{\lambda_0^2}\frac{E_i^2}{d_{SR}^2} G A_{refl}^2 e_s}{E_i^2} = \frac{4\pi}{\lambda_0^2} A_{refl}^2 G e_s \tag{C4}$$

APPENDIX D. DERIVATION OF THE REFLECTED PATH SCALING

At the receiver antenna, power P_{Rx} of the finite-area reflector scattered path is determined by effective area of the antenna $G_{Rx} \cdot A_{omni}$ and power density S_s of the scattered field E_s, which relate to each other by the well-known radio transmission formulas:

$$|C_{TSR}| = \sqrt{\frac{P_{Rx}}{P_{Tx} G_{Tx} G_{Rx}}} \tag{D1}$$

$$P_{Rx} = A_{Rx} S_s \tag{D2}$$

$$A_{Rx} = A_{omni} G_{Rx} = \frac{\lambda_0^2}{4\pi} G_{Rx} \tag{D3}$$

$$S_s = \frac{|E_s|^2}{\eta_0} \tag{D4}$$

Expressing the abs square of the scattered field in (B8) in terms of radar cross-section of Eq. (C4) we obtain:

$$|E_s|^2 = \frac{4\pi}{d_{SR}^2} |E_i|^2 \sigma_{D,A}^{\mathbf{e}_D,\mathbf{e}_A} \tag{D5}$$

Next, inserting (D5) into (D4), (D4) and (D3) into (D1) we obtain:

$$|C_{TSR}^{\mathbf{e}_D,\mathbf{e}_A}| = \frac{\lambda_0}{4\pi d_{SR} d_{TS}} \sqrt{\frac{\sigma_{D,A}^{\mathbf{e}_D,\mathbf{e}_A}}{4\pi}} \tag{D6}$$

To express the combined channel path conveniently in terms of product of Tx-surface and surface-Rx path as in Eq. 3, we need to consider paths amplitudes normalization factors shown in (2).

$$C_{TS}^{\mathbf{e}_D,\mathbf{e}_A} = \frac{-j\lambda_0}{4\pi} \frac{e^{-j\beta_0 d_{A,c}}}{d_{TS}} \tag{D7}$$

$$C_{SR}^{\mathbf{e}_D,\mathbf{e}_A} = \frac{-j\lambda_0}{4\pi} \frac{e^{-j\beta_0 d_{D,c}}}{d_{SR}} \tag{D8}$$

$$R^{\mathbf{e}_D,\mathbf{e}_A} = \frac{C_{TSR}^{\mathbf{e}_D,\mathbf{e}_A}}{C_{TS}^{\mathbf{e}_D,\mathbf{e}_A} C_{SR}^{\mathbf{e}_D,\mathbf{e}_A}} \tag{D9}$$

Inserting Eqs. (D8), (D7), and (D6) into (D9) results in Eq. (5), concluding the proof.

APPENDIX E. LOCAL PHASE RESPONSE CONCEPT JUSTIFICATION FOR META-REFLECTORS

To derive the semi-closed form expression for a reflection from a meta-reflector, we start from (C3) and using linearity of the integral, write double integration over the whole surface as a sum of integrals over finite number N_c of unit cells:

$$\iint_{A_{refl}} \psi_{D,c}\psi_{A,c} da = \sum_{c=1}^{N_c} \iint_{a_c} \psi_{D,c}\psi_{A,c} da \tag{E1}$$

Assuming that the phase factor within integrals is monotonic over a single sub-half-wavelength unit cell area, we use the mean value theorem for integrals taking values of the function at the center of the unit cell given by x_c, y_c, z_c and introduce a complex-valued factor w_c, which will account for difference between function value at the center of the cell and that at the unknown point of the theorem — at the coordinate where the integral value is equal to the value at the cell center.

$$\iint_{a_c} \psi_{D,c}\psi_{A,c} da = \psi_{D,c}\psi_{A,c} \iint_{a_c} dw = \psi_{D,c}\psi_{A,c} w_c \tag{E2}$$

The illustration of the local phase response concept is given in Fig. E1.

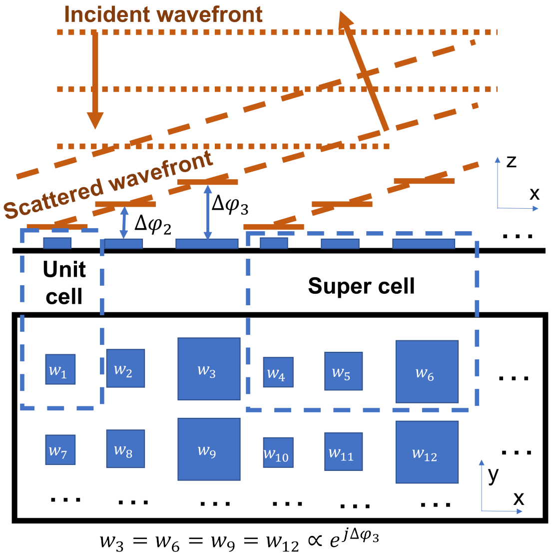

FIGURE E1. A scheme of the meta-reflector for semi-analytical model of RCS. Each unit cell of unique type imposes a unique phase shift on the incident wave. For periodic reflectors a repeating sequence of unit cells is a super-cell.

REFERENCES

[1] Wu, Q., S. Zhang, B. Zheng, C. You, and R. Zhang, "Intelligent reflecting surface-aided wireless communications: A tutorial," *IEEE Transactions on Communications*, Vol. 69, No. 5, 3313–3351, 2021.

[2] Yuan, Y., Y. Huang, and F.-L. Luo, *Metasurfaces for Wireless Communications: Designs and Implementations*, 1st ed., CRC Press, 2024.

[3] Khawaja, W., O. Ozdemir, Y. Yapici, F. Erden, and I. Guvenc, "Coverage enhancement for NLOS mmWave links using passive reflectors," *IEEE Open Journal of the Communications Society*, Vol. 1, 263–281, 2020.

[4] Wireless InSite® 3D Wireless Propagation Software, https://www.remcom.com/wireless-insite-propagation-software.

[5] Gu, Q., D. Wu, X. Su, H. Wang, J. Cui, and Y. Yuan, "System-level simulation of reconfigurable intelligent surface assisted wireless communications system," *ArXiv Preprint ArXiv:2206.14777*, 2022.

[6] Özdogan, O., E. Björnson, and E. G. Larsson, "Intelligent reflecting surfaces: Physics, propagation, and pathloss modeling," *IEEE Wireless Communications Letters*, Vol. 9, No. 5, 581–585, 2019.

[7] Chia, T.-T., "Prediction of electromagnetic scattering from metasurfaces," in *2016 10th European Conference on Antennas and Propagation (EuCAP)*, 1–5, Davos, Switzerland, Apr. 2016.

[8] Díaz-Rubio, A. and S. A. Tretyakov, "Macroscopic modeling of anomalously reflecting metasurfaces: Angular response and far-field scattering," *IEEE Transactions on Antennas and Propagation*, Vol. 69, No. 10, 6560–6571, 2021.

[9] Wang, X., A. Díaz-Rubio, V. S. Asadchy, G. Ptitcyn, A. A. Generalov, J. Ala-Laurinaho, and S. A. Tretyakov, "Extreme asymmetry in metasurfaces via evanescent fields engineering: Angular-asymmetric absorption," *Physical Review Letters*, Vol. 121, No. 25, 256802, 2018.

[10] Díaz-Rubio, A., S. Kosulnikov, and S. A. Tretyakov, "On the integration of reconfigurable intelligent surfaces in real-world environments: A convenient approach for estimation reflection and transmission," *IEEE Antennas and Propagation Magazine*, Vol. 64, No. 4, 85–95, 2022.

[11] Liu, Y., Z. Liu, S. V. Hum, and C. D. Sarris, "An equivalence principle-based hybrid method for propagation modeling in radio environments with reconfigurable intelligent surfaces," *IEEE Transactions on Antennas and Propagation*, Vol. 72, No. 7, 5961–5973, Jul. 2024.

[12] 3GPP ETSI TR 138.901, "Study on channel model for frequencies from 0.5 to 100 GHz," Jan. 2020.

[13] Vitucci, E. M., M. Fabiani, and V. Degli-Esposti, "Use of a realistic ray-based model for the evaluation of indoor RF coverage solutions using reconfigurable intelligent surfaces," *Electronics*, Vol. 12, No. 5, 1173, 2023.

[14] Liu, Y. and C. D. Sarris, "Efficient computation of scattered fields from reconfigurable intelligent surfaces for propagation modeling," *IEEE Transactions on Antennas and Propagation*, Vol. 72, No. 2, 1817–1826, Feb. 2024.

[15] Nayeri, P., A. Z. Elsherbeni, and F. Yang, "Radiation analysis approaches for reflectarray antennas [antenna designer's notebook]," *IEEE Antennas and Propagation Magazine*, Vol. 55, No. 1, 127–134, Feb. 2013.

[16] Jaeckel, S., L. Raschkowski, L. Thiele, *et al.*, "Quasi deterministic radio channel generator user manual and documentation," *Fraunhofer Heinrich Hertz Institute Wireless Communications and Networks*, 1–4, 2016.

[17] Sun, S., "Channel modeling and multi-cell hybrid beamforming for fifth-generation millimeter-wave wireless communications," Ph.D. dissertation, New York University, New York, USA, 2018.

[18] Weiler, R. J., M. Peter, W. Keusgen, A. Maltsev, I. Karls, A. Pudeyev, I. Bolotin, I. Siaud, and A.-M. Ulmer-Moll, "Quasi-deterministic millimeter-wave channel models in MiWEBA," *EURASIP Journal on Wireless Communications and Networking*, Vol. 2016, 1–16, Mar. 2016.

[19] Liu, L., C. Oestges, J. Poutanen, K. Haneda, P. Vainikainen, F. Quitin, F. Tufvesson, and P. D. Doncker, "The COST 2100 MIMO channel model," *IEEE Wireless Communications*, Vol. 19, No. 6, 92–99, 2012.

[20] Orfanidis, S. J., *Electromagnetic Waves and Antennas*, Rutgers University, NJ, USA, 2003.

[21] Amiot, N., M. Laaraiedh, and B. Uguen, "Pylayers: An open source dynamic simulator for indoor propagation and localization," in *2013 IEEE International Conference on Communications Workshops (ICC)*, 84–88, Budapest, Hungary, Jun. 2013.

[22] Amiot, N., "Design of simulation platform joigning site specific radio propagation and human mobility for localization applications," Ph.D. dissertation, University of Rennes, Rennes, France, 2013.

[23] PyLayers GitHub repository, https://github.com/pylayers/pylayers.

[24] Hoydis, J., S. Cammerer, F. A. Aoudia, A. Vem, N. Binder, G. Marcus, and A. Keller, "Sionna: An open-source library for next-generation physical layer research," *ArXiv Preprint ArXiv:2203.11854*, 2022.

[25] Aubert, L.-M., B. Uguen, and F. T. Talom, "Deterministic simulation of MIMO–UWB transmission channel," *Comptes Rendus Physique*, Vol. 7, No. 7, 751–761, 2006.

[26] Balanis, C. A., *Advanced Engineering Electromagnetics*, John Wiley & Sons, 2012.

[27] Ansys HFSS, "3D Electromagnetic Field Simulator for RF and Wireless Design," https://www.ansys.com/products/electronics/ansys-hfss.

[28] Tretyakov, S., *Analytical Modeling in Applied Electromagnetics*, Artech House, 2003.

[29] Oskooi, A. F., D. Roundy, M. Ibanescu, P. Bermel, J. D. Joannopoulos, and S. G. Johnson, "MEEP: A flexible free-software package for electromagnetic simulations by the FDTD method," *Computer Physics Communications*, Vol. 181, No. 3, 687–702, 2010.

[30] Kashyap, B. G., P. C. Theofanopoulos, Y. Cui, and G. C. Trichopoulos, "Mitigating quantization lobes in mmwave low-bit reconfigurable reflective surfaces," *IEEE Open Journal of Antennas and Propagation*, Vol. 1, 604–614, 2020.

[31] Hwang, R.-B., *Periodic Structures: Mode-Matching Approach and Applications in Electromagnetic Engineering*, John Wiley & Sons, 2012.